First Sub-parsec-scale Mapping of Magnetic Fields in the Vicinity of a Very-low-luminosity Object, L1521F-IRS

Soam, Archana

2019-09-20

Soam , A , Lee , C W , Andersson , B-G , Maheswar , G , Juvela , M , Liu , T , Kim , G , Rao , R , Chung , E J , Kwon , W & Ekta , S 2019 , ' First Sub-parsec-scale Mapping of Magnetic Fields in the Vicinity of a Very-low-luminosity Object, L1521F-IRS ' , Astrophysical Journal , vol. 883 , no. 1 , 9 . https://doi.org/10.3847/1538-4357/ab365d

http://hdl.handle.net/10138/309270
https://doi.org/10.3847/1538-4357/ab365d

publishedVersion

The Astrophysical Journal, 883:9 (9pp), 2019 September 20 https://doi.org/10.3847/1538-4357/ab365d

First Sub-parsec-scale Mapping of Magnetic Fields in the Vicinity of a Very-low-luminosity Object, L1521F-IRS

Archana Soam[1,2], Chang Won Lee[2,3], B-G Andersson[1], G. Maheswar[4], Mika Juvela[5], Tie Liu[6,2,7], Gwanjeong Kim[8], Ramprasad Rao[9], Eun Jung Chung[2,10], Woojin Kwon[2,3], and S. Ekta[4]
[1] SOFIA Science Centre, USRA, NASA Ames Research Centre, MS-12, N232, Moffett Field, CA 94035, USA; archanasoam.bhu@gmail.com, asoam@usra.edu
[2] Korea Astronomy and Space Science Institute (KASI), 776 Daedeokdae-ro, Yuseong-gu, Daejeon 34055, Republic of Korea
[3] University of Science and Technology, Korea (UST), 217 Gajeong-ro, Yuseong-gu, Daejeon 34113, Republic of Korea
[4] Indian Institute of Astrophysics, Kormangala (IIA), Bangalore 560034, India
[5] Department of Physics, P.O. Box 64, FI-00014, University of Helsinki, Finland
[6] Shanghai Astronomical Observatory, Chinese Academy of Sciences, 80 Nandan Road, Shanghai 200030, People's Republic of China
[7] East Asian Observatory, 660 N. A'ohōkū Place, University Park, Hilo, HI 96720, USA
[8] Nobeyama Radio Observatory, National Astronomical Observatory of Japan, National Institutes of Natural Sciences, Nobeyama, Minamimaki, Minamisaku, Nagano 384-1305, Japan
[9] Academia Sinica Institute of Astronomy and Astrophysics, P.O. Box 23-141, Taipei 10617, Taiwan
[10] Department of Astronomy and Space Science, Chungnam National University, 99 Daehak-ro, Yuseong-gu, Daejeon 34134, Republic of Korea
Received 2019 April 2; revised 2019 July 2; accepted 2019 July 27; published 2019 September 17

Abstract

L1521F is found to be forming multiple cores and it is cited as an example of the densest core with an embedded VeLLO in a highly dynamical environment. We present the core-scale magnetic fields (*B*-fields) in the near vicinity of the VeLLO L1521F-IRS using submillimeter polarization measurements at 850 μm using JCMT POL-2. This is the first attempt to use high-sensitivity observations to map the sub-parsec-scale *B*-fields in a core with a VeLLO. The *B*-fields are ordered and very well connected to the parsec-scale field geometry seen in our earlier optical polarization observations and the large-scale structure seen in *Planck* dust polarization. The core-scale *B*-field strength estimated using the Davis–Chandrasekhar–Fermi relation is 330 $\pm$ 100 μG, which is more than 10 times the value we obtained in the envelope (the envelope in this paper is the "core envelope"). This indicates that *B*-fields are getting stronger on smaller scales. The magnetic energies are found to be 1 to 2 orders of magnitude higher than nonthermal kinetic energies in the envelope and core. This suggests that magnetic fields are more important than turbulence in the energy budget of L1521F. The mass-to-flux ratio of 2.3 $\pm$ 0.7 suggests that the core is magnetically supercritical. The degree of polarization is steadily decreasing toward the denser part of the core with a power-law slope of −0.86.

Unified Astronomy Thesaurus concepts: Star formation (1569); Polarimetry (1278); Interstellar clouds (834); Interstellar magnetic fields (845)

1. Introduction

Magnetic fields (*B*-fields) are found to be one of the important drivers in the star formation process but they are not very well constrained by available observations. The influence of *B*-fields on various spatial scales and stages of star formation is still unclear. Both magnetically dominated and turbulence dominated scenarios have been advocated to explain the fact that star formation is slow compared to freefall times (Krumholz et al. 2005; Tan et al. 2006). In the magnetically dominated scenario for isolated low-mass star formation, the cores gradually condense out of a magnetically subcritical background cloud, through ambipolar diffusion (Shu et al. 1987a; McKee et al. 1993; Mouschovias & Ciolek 1999; Allen et al. 2003). In this process, the material, mediated by the magnetic field lines, settles into a disk-like morphology of a few thousand astronomical units in size. This allows the cloud-scale magnetic fields to become parallel to the cloud minor axis. Turbulence-dominated scenarios will produce less orderly magnetic field configurations.

The *B*-fields are mapped using well established technique of polarization measurements. In the shorter wavelengths (i.e., optical and near-infrared), the dichroism or selective extinction causes the observed polarization. The polarization position angles in optical wavelengths trace the plane-of-sky orientation of the ambient magnetic field at the periphery of molecular clouds (with $A_V \approx$ 1–2 mag; Goodman et al. 1995; Goodman 1996). The minor axes of dust grains align with the orientation of magnetic fields (Hoang & Lazarian 2008). Polarization observations at submillimeter/millimeter wavelengths are used to trace the field lines in more dense regions of the cloud (Ward-Thompson et al. 2009). The thermal emission from the dust grains is stronger along the major axis, producing a polarization direction perpendicular to the magnetic fields in the denser core regions ($n_{H_2} \sim 10^5$–10^6 cm^{-3}) observable even with $A_V > 50$ mag. The line-of-sight component of the magnetic field is measured using Zeeman observations (Crutcher et al. 1993).

L1521F (MC27; Codella et al. 1997; Onishi et al. 1999; Lee et al. 2001) is located in the Taurus star-forming region at a distance of 140 pc (Loinard et al. 2005; Torres et al. 2007). This core contains a very-low-luminosity object (VeLLO) L1521F-IRS with bolometric luminosity of $L = 0.05\ L_\odot$ (Bourke et al. 2006; Terebey et al. 2006). The source was discovered by the *Spitzer Space Telescope* (*SST*; Bourke et al. 2006) but could not be detected in the *IRAS* mission (Beichman et al. 1986; Benson & Myers 1989; Codella et al. 1997) due to its low luminosity. The core appears to be isolated and associated with strong central condensation in the 160 μm *Spitzer* image (Kirk et al. 2007) but recent ALMA observations using high-density tracers reveal that this is a possible site of multiple star formation (Tokuda et al. 2014). The embedded VeLLO L1521F-IRS is found to be associated with a compact

but poorly collimated molecular outflow in CO($J = 2$–1) line observations (Takahashi et al. 2013). Moreover, Tokuda et al. (2014) found a very compact bipolar outflow centered at L1521F-IRS using HCO^+ ($J = 3$–2) observations from ALMA. This core is considered to be at a very early stage of star formation based on recent ALMA observations of dust continuum emission and molecular rotational lines by Tokuda et al. (2016). In a latest study of the CO outflow survey of 68 VeLLOs, Kim et al. (2019) suggest that L1521F-IRS is a potential proto-brown dwarf candidate. They reported the largest identified sample of 15 proto-brown dwarfs among 68 VeLLOs. Their segregation is based on the smaller envelope masses and lower accretion rates estimated from CO, ^{13}CO, and C^{18}O molecular line observations.

VeLLOs ($L_{\rm int} \lesssim 0.1\,L_\odot$) have been detected based on the data from the *SST*. The VeLLOs are interesting sources as their luminosity is an order of magnitude lower than the accretion luminosity $L_{\rm acc} \sim 1.6\,L_\odot$ expected for a $0.08\,M_\odot$ protostar with an accretion rate of $\sim 10^{-6}\,M_\odot\,{\rm yr}^{-1}$ (Shu et al. 1987b) and $3R_\odot$ stellar radius. It has been speculated that these sources are either progenitors of proto-brown dwarfs (e.g., Lee et al. 2013; Liu et al. 2016) or very-low-mass protostars.

The outflows from the protostars are thought to influence their surrounding environment by generating turbulence that could scramble a relatively weak magnetic field in their vicinity. This could disturb any initial alignment between the core and the envelope magnetic fields. On the other hand, the estimated outflow parameters suggest that VeLLOs have the most compact, lowest mass, and least energetic outflows compared to known Class 0/I outflows from low-mass stars (e.g., Belloche et al. 2002; Wu et al. 2004; Bourke et al. 2006; Pineda et al. 2011). We therefore expect the outflows from these sources to have the least significant effect on their surroundings. This would enable the regions to preserve the initial condition that may have existed prior to the initiation of star formation showing primordial magnetic fields.

Here we present the first high-sensitivity submillimeter polarization observations made toward the L1521F core harboring a VeLLO with the Submillimetre Common-User Bolometer Array 2 (SCUBA-2) camera with the POL-2 polarimeter commissioned at James Clarke Maxwell Telescope (JCMT). The mapping of sub-parsec-scale *B*-fields toward a low-mass star-forming core (with a VeLLO or proto-brown dwarf candidate) in a highly dynamical environment is presented for the first time in the present study. The line-of-sight magnetic field toward this source is already studied by Crutcher et al. (2010). The molecular line observations toward this region using the Heterodyne Array Receiver Program (HARP; Carney et al. 2016) and Atacama Large millimeter/submillimeter Array (ALMA; Tokuda et al. 2014, 2016) are already available to understand the kinematics of the core.

The paper is organized as follows: in Section 2, we describe the observations and data reduction; in Section 3, we give initial results; in Section 4, we discuss and summarize our results.

2. Data Acquisition and Reduction Techniques

We observed L1521F in 850 μm polarized emission with SCUBA-2 (Holland et al. 2013) in conjunction with POL-2 (Friberg et al. 2016; P. Bastien et al. 2019, in preparation) on the nights of 2017 November 11–14 under the project code M17BP070 (PI: Soam A.) at JCMT. L1521F was mapped with 18 observations, with an average integration time of ∼0.55 hr per observation, in good weather ($0.05 < \tau_{225} < 0.08$, where τ_{225} is atmospheric opacity at 225 GHz). A POL-2 daisy (Friberg et al. 2016) scan pattern was used for mapping the core producing a uniform, high signal-to-noise coverage over the central 3′ of the map. This pattern is similar to the SCUBA-2 CV daisy scan pattern (Holland et al. 2013) but modified to have a slower scan speed (8″/s compared to 155″/s) to obtain sufficient on-sky data for good Stokes *Q* and *U* values. A fully sampled mapping was done in a 12′ diameter, circular region with an effective resolution of 14.″1. The frequency of wave-plate rotation was 2 Hz.

For reducing the data, we used the `pol2map` python script in the Starlink (Currie et al. 2014)[11] `SMURF` (Jenness et al. 2013) package. Starlink tasks such as `calcqu` and `makemap` (Chapin et al. 2013) were used in the reduction process. The detailed procedure to reduce the data and to produce the polarization catalog is explained in Kwon et al. (2018) and Soam et al. (2018). We adopted a slightly different reduction procedure by using an additional parameter `skyloop` in `pol2map` setting the pixel size as 12″. See Mairs et al. (2015) and Kwon et al. (2018) for a more detailed description of the SCUBA-2 and POL-2 data reduction processes, respectively. The vectors are debiased (Kwon et al. 2018) to remove the effect of statistical biasing in low signal-to-noise-ratio (S/N) regions. Polarized values are obtained by combining *Q* and *U* maps where polarized intensity exceeds two times its standard deviation. For analyzing the data, we have used only those detections where S/N > 2 in polarized intensity and polarization fraction. All position angles are measured from north increasing toward east. Magnetic field orientation is derived by rotating the polarization angles by 90°.

3. Results and Discussion

3.1. Structure and Kinematics of L1521F

Figure 1 shows the dust continuum emission maps of L1521F observed from *Herschel*/SPIRE at 250, 350, and 500 μm wavelengths and JCMT/SCUBA-2 observations at 850 μm wavelength (this work). SCUBA-2 has a spatial resolution of 14″, i.e., ∼2000 au spatial scale at a distance of L1521F, i.e., 140 pc. The peak values of total and polarized intensities are found to be ∼200 mJy beam^{-1} and ∼15 mJy beam^{-1}, respectively. The rms noise of the background region in the Stokes *I* map is measured to be ∼2.5 mJy beam^{-1}. This value was estimated by selecting a region with relatively constant signal ∼1′ away from the center of the Stokes *I* map. This region is relatively flat, moderately unpolarized, low in emission, and away from the brightest region in the *I* map. The standard deviation of the measured flux density distribution in that region is considered to be the rms of the Stokes *I* map.

The L1521F core seems to be elongated in the north and south. The 850 μm observation indicates two curved emission features that seem to be coming out of the core in the northward direction and one of them is bending westward. These features are indicated by dashed lines in the lower right panel of Figure 1. Interestingly, the similar core structure can be noted in *Herschel*/SPIRE images shown in upper left, upper right, and lower left panels of Figure 1 at different wavelengths. The

[11] *Software:* Starlink (Currie et al. 2014), SMURF (Jenness et al. 2013) used in POL-2 data reduction is currently supported by the East Asian Observatory.

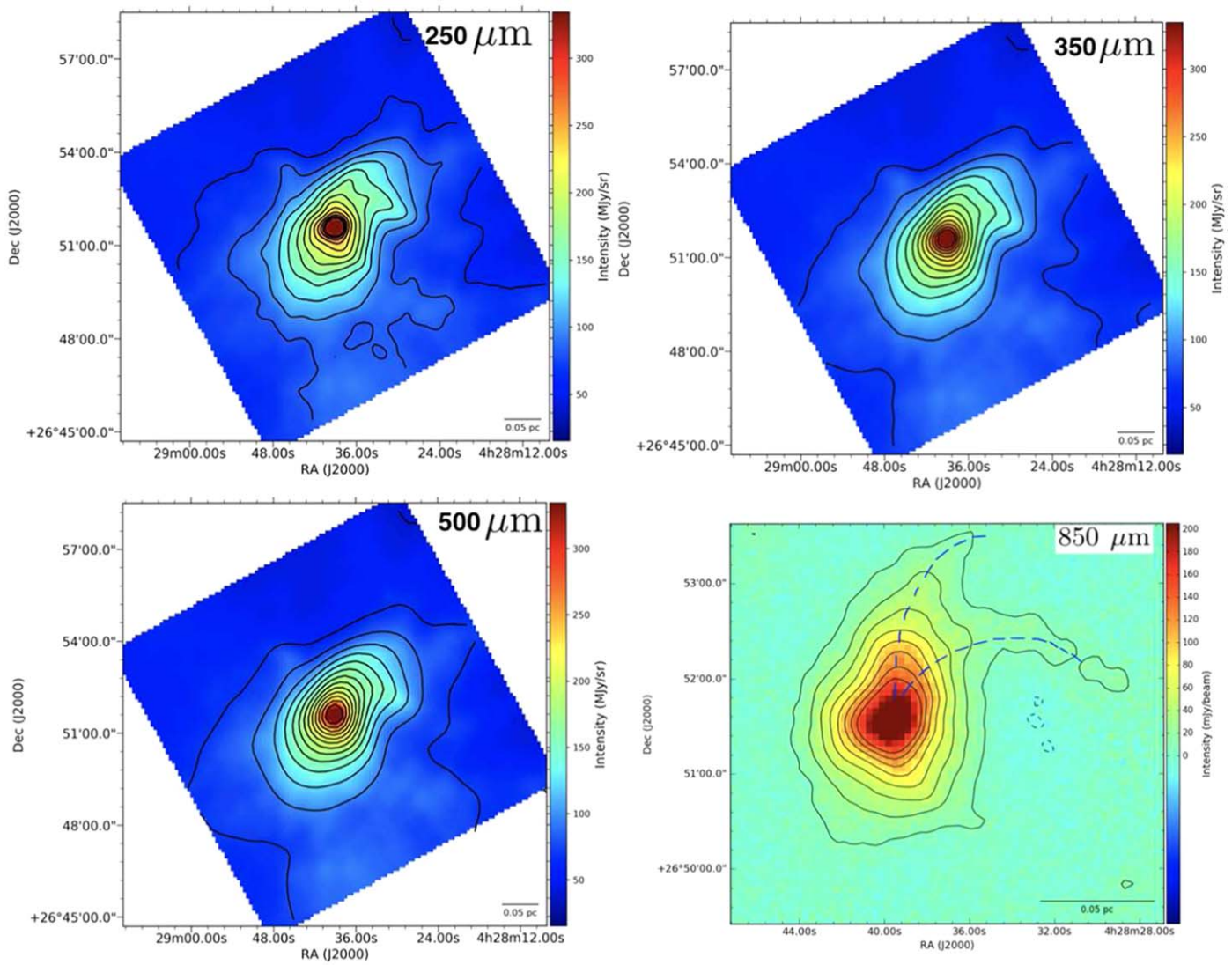

Figure 1. Dust emission maps of L1521F seen at 250, 350, and 500 μm wavelengths by *Herschel*/SPIRE and at 850 μm by JCMT/SCUBA-2. Contours of 850 μm intensity are shown with levels 8, 10, 45, 80, 105, 140 mJy beam^{-1}. The two interesting features seen at 850 μm are indicated with blue dashed lines.

results of JCMT/POL-2 polarization observations are given in Table 1.

Lee et al. (1999) classified the L1521F core as an infall candidate based on their high-resolution observations of CS ($J = 2$–1), which is supported by Onishi et al. (1999) from their HCO^+ ($J = 3$–2) and ($J = 4$–3) observations. The CS ($J = 2$–1) and N_2H^+ ($J = 1$–0) maps of L1521F shown by Lee et al. (2001), however, indicate an extended red asymmetry over the core region. The formation of L1521F-IRS can be correlated with these motions seen by Lee et al. (2001).

L1521F is found to be embedded in a very interesting and dynamic environment seen by the ALMA HCO^+ ($J = 3$–2) observations by Tokuda et al. (2014). The compact bipolar outflow seen in their HCO^+ ($J = 3$–2) map at ~500 au scale shows some dynamical interaction with the surrounding gas. There are two high-density cores detected in both dust continuum emission and $H^{13}CO^+$ ($J = 3$–2). The observed features seen in the HCO^+ ($J = 3$–2) and $H^{13}CO^+$ ($J = 3$–2) lines by Tokuda et al. (2014) suggest that L1521F is probably embedded in a site where multiple stars are being formed. Tokuda et al. (2016) presented ALMA observations of dust continuum emission and molecular rotational lines toward L1521F. The two starless cores in the close vicinity of L1521F are found and complex gas structure is seen in ^{12}CO($J = 3$–2) and HCO^+($J = 3$–2) observations. An arc-like feature and a few other core features connected to L1521F are noticed in HCO^+ ($J = 3$–2) emission. The length of the arc-like structure was found to be ~2000 au. They considered this arc-like structure to be a possible result of dynamical interaction between the small dense cores and the surrounding gas on an ~2000 au scale.

The two diffused features coming out of the L1521F core in 850 μm and Herschel images (see Figure 1) are not quite related to either the observed magnetic field morphology or the outflow cavity in the L1521F core (see Figure 2). This could be one of several such structures seen toward the Taurus molecular clouds. Several of these structures show similar east–west patterns; for example, the structures seen in the direction of other L1521 cores (A, B, E, etc.) suggest some sort of external influence. Recently, Shimajiri et al. (2019) showed a possible scenario where the gas motion toward the B213 filament is due to its interaction with Per OB2 association. Authors propose that the B211/B213 filament was initially formed by large-scale compression of H I gas by Per OB2

Table 1
Results of JCMT/POL-2 Observations toward L1521F at 850 μm Wavelength

Id	α (J2000) (°)	δ (J2000) (°)	$I \pm \sigma_I$ (mJy/beam)	$P \pm \sigma_P$ (%)	$\theta \pm \sigma_\theta$ (°)
1	67.164	26.848	136.6 ± 3.1	12.6 ± 3.6	−75.8 ± 10.3
2	67.160	26.848	105.8 ± 1.8	8.3 ± 3.7	−89.4 ± 9.5
3	67.156	26.848	54.5 ± 2.2	14.8 ± 6.4	−82.7 ± 7.3
4	67.164	26.851	100.4 ± 5.3	5.5 ± 1.9	−64.3 ± 9.2
5	67.160	26.851	81.7 ± 2.7	11.0 ± 1.8	−74.6 ± 4.9
6	67.156	26.851	53.1 ± 1.3	14.1 ± 4.6	−82.9 ± 12.4
7	67.171	26.855	128.3 ± 1.8	3.1 ± 1.4	−44.4 ± 11.9
8	67.164	26.855	176.3 ± 2.7	2.9 ± 0.8	−61.8 ± 7.8
9	67.160	26.855	105.3 ± 1.9	3.6 ± 1.3	−87.8 ± 9.8
10	67.153	26.858	42.5 ± 1.0	15.8 ± 7.8	−52.5 ± 12.1
11	67.175	26.861	95.3 ± 2.2	9.5 ± 4.4	−39.8 ± 11.0
12	67.171	26.861	143.0 ± 1.4	4.7 ± 1.6	−66.0 ± 9.2
13	67.175	26.865	55.1 ± 2.1	23.8 ± 9.9	−51.6 ± 9.8
14	67.171	26.865	92.4 ± 2.5	8.7 ± 3.4	−59.8 ± 9.3
15	67.168	26.865	115.0 ± 1.1	3.8 ± 1.2	−32.5 ± 9.6
16	67.171	26.868	72.6 ± 1.5	10.8 ± 4.8	−63.8 ± 10.5
17	67.168	26.868	98.5 ± 2.7	5.2 ± 2.1	−22.0 ± 10.6
18	67.164	26.868	123.4 ± 2.1	3.3 ± 1.6	−42.9 ± 12.1

Note. θ is the polarization position angle before rotating by 90°.

association and then it is growing due to gravitational accretion of the ambient cloud. L1521F is one of several cores embedded in the Taurus molecular cloud and may be undergoing the process of gravitational accretion of surrounding material.

3.2. Magnetic Field Morphology

Figure 2 shows the *B*-field morphology in L1521F obtained from *Planck* 850 μm, optical *R*-band (0.63 μm) and JCMT/POL-2 850 μm observations. The parsec-scale *B*-field geometries are shown in panels (a) and (b), and the core field geometry at the subparsec scale is zoomed-in in panel (c). The location of L1521F-IRS and the associated bipolar outflows is shown with star and double-headed arrow symbols in panels (b) and (c). Figure 3 shows the Gaussian fitted histogram to the distribution of plane-of-sky *B*-field position angles measured in optical and submillimeter observations. The mean and standard deviation values are found to be similar in both the distributions. The lower panel of the same figure shows the distributions of polarization fraction and position angle values detected in the envelope and core of L1521F. The maximum amount of polarization seen in the diffuse envelope and dense core of L1521F are found to be ∼7 ± 2% and ∼24 ± 10%, respectively. However, the pattern of distribution seems similar in both cases.

Dust polarization in *Planck* 850 μm observations is used to investigate the *B*-field morphology at a scale of 5′ (Planck Collaboration et al. 2016). The image in panel (a) of Figure 2 is smoothed down to the 7′ resolution to ensure good S/N data. The vectors are drawn at 3.′5 (half-resolution) steps. The figure shows the large-scale magnetic fields toward L1521F. The location of L1521F is shown by the white ellipse indicating the area covered by SCUBA-2 observations. The large-scale field seems to be running from northeast to southwest. However, at the location of L1521F, the field lines are mainly seen in the north–south direction. A smooth bending in the field lines can be seen from the southwest to north direction. The pinching of field lines is perceptible in the region east of L1521F. This region also shows a higher degree of polarization than that seen in L1521F. A similar trend of field lines was observed by Soam et al. (2015) when they plotted the optical polarization vectors with the Heiles catalog (Heiles 2000) data selected within 1° radius around L1521F (see Figure 8 of Soam et al. 2015).

The field geometry in the L1521F envelope seen from optical observations is zoomed-in in panel (b) of Figure 2 (Soam et al. 2015). The mean orientation of field lines is from the northeast to southwest direction, which seems consistent with that seen in *Planck* observations. The field lines appear organized but not aligned with the outflow direction.

The *B*-field geometry is investigated in L1521F from POL-2 850 μm observations by further zooming-in (panel (c) of Figure 2). Interestingly, the northeast to southwest component is still seen in the map. The difference between the outflow direction and the magnetic field orientation in the envelope is ∼50° (Soam et al. 2015). The core-scale *B*-fields are also misaligned with an offset of ∼48° between outflows and mean magnetic field orientation. However, field lines are more aligned with outflows if the northeastern component only is taken into account.

The maps seen at three different scales suggest that field lines on envelope and core scales are connected and the global *B*-field orientation is from northeast to southwest. This connection is also depicted in the histograms of position angles plotted in Figure 3. Both populations peak between ∼0–40°. The correlation of optical and submillimeter observations can further suggest that the core is embedded in the strong magnetic field environment.

An interesting feature of bending in field lines can be seen in the core-scale *B*-field geometry. This is further demonstrated in Figure 4 where the elliptical core and field lines are shown. The location of embedded source in the core is shown with a star symbol. The associated bipolar outflow cavities are indicated with dashed parabolas based on the *Spitzer* observations of this source by Bourke et al. (2006) shown in the color-composite image as inset in the upper-right corner of this figure. The field lines in this cartoon seem to be the result of the northeast to southwest orientation of *Planck* and optical polarization observations, which gets bent in the core seen at submillimeter wavelength.

3.3. Strength of Magnetic Fields

We used the Davis–Chandrasekhar–Fermi method (hereafter DCF method; Davis 1951; Chandrasekhar & Fermi 1953) for field strength estimation in the L1521F core. The modified DCF relation (Crutcher et al. 2004) for measuring the plane-of-sky *B*-field ($B_{\rm pos}$) strength is:

$$B_{\rm pos} = Q'\sqrt{4\pi\rho}\,\frac{\sigma_v}{\delta\theta} \approx 9.3\sqrt{n({\rm H_2})}\,\frac{\Delta v}{\delta\theta}\ \mu{\rm G}, \qquad (1)$$

where Q' accounts for variation in field strength on scales smaller than beam and is taken as a factor of order unity (Crutcher et al. 2004). The value of Q' here is used as 0.5 (Ostriker et al. 2001). The $\rho = \mu_g m_{\rm H} n({\rm H_2})$ is the gas density where $\mu_g = 2.8$ is the mean molecular weight of the gas (Kauffmann et al. 2008), $m_{\rm H}$ is the mass of a hydrogen atom, and $n({\rm H_2})$ is the number density of molecular hydrogen in cm^{-3}. In Equation (1), $\Delta v = \sigma_v\sqrt{8\ln 2}$ is FWHM in km s^{-1}, where σ_v is the average line-of-sight nonthermal velocity dispersion, $\delta\theta$ is corrected dispersion in position angle in degrees. The corrected dispersion in position angle is obtained

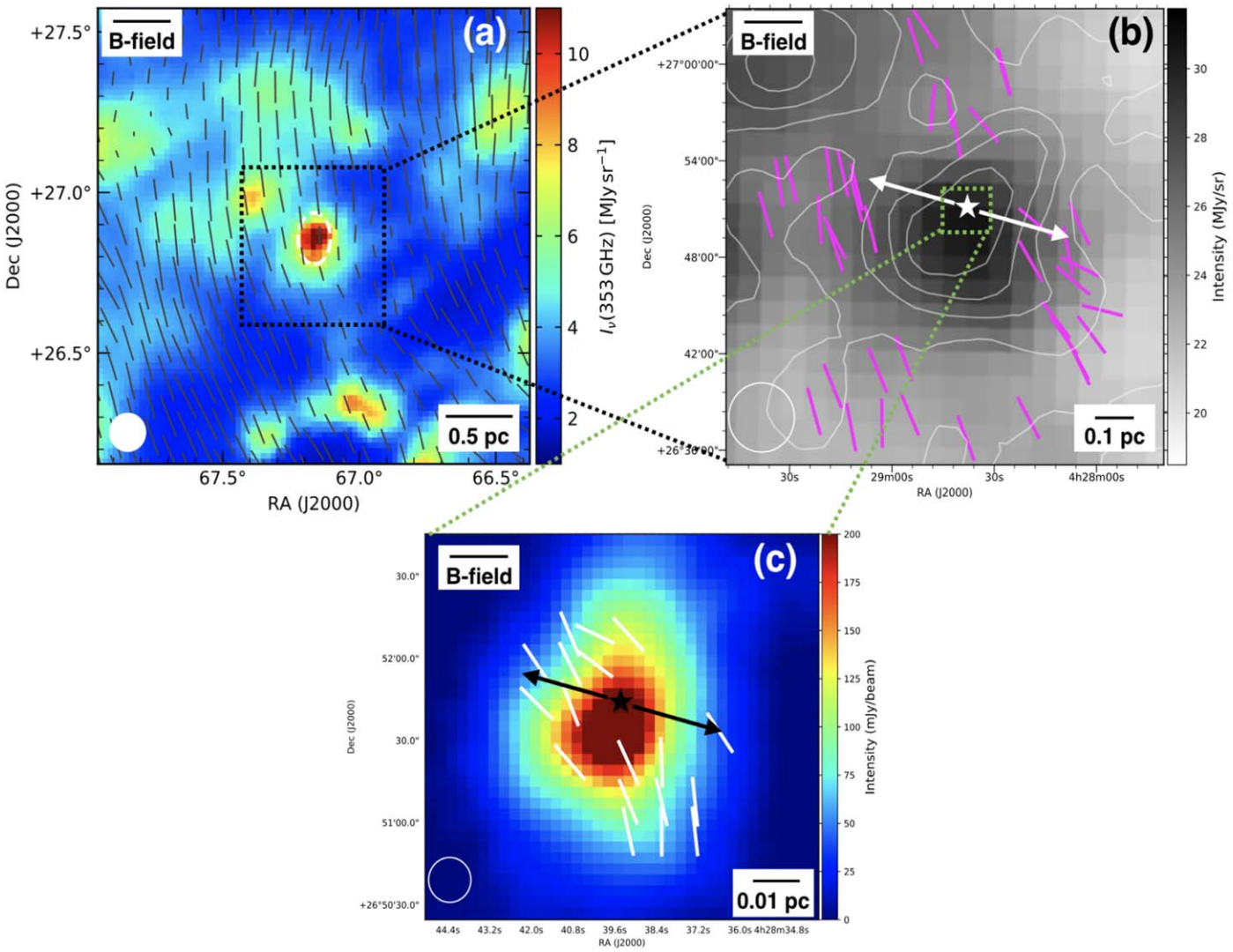

Figure 2. Panel (a): morphology of *B*-fields obtained from *Planck* 850 μm dust polarization observations. The location of L1521F is shown with a dashed ellipse in the center. Panel (b): the *B*-fields mapped with optical *R*-band (0.63 μm) observations by Soam et al. (2015) plotted on *IRAS* 100 μm with the contours of Dobashi extinction map of L1521F (Dobashi et al. 2005). The position of VeLLO and associated CO bipolar outflows (Takahashi et al. 2013) are shown with a star symbol and a double-headed arrow. Panel (c): the *B*-field morphology obtained from 850 μm dust polarization observations of L1521F core shown on 850 μm dust continuum map. The lengths of line segments are normalized and independent of fraction of polarization. The beam sizes in all the frames are shown with filled and open circles.

by adopting the procedure explained by Lai et al. (2001) and Franco et al. (2010) where correction is done in quadrature by using $\delta\theta = (\sigma_{\rm std}{}^2 - \langle\sigma_\theta\rangle^2)^{1/2}$, where $\sigma_{\rm std}$ is the standard deviation in the distribution of position angle and the mean uncertainty $\langle\sigma_\theta\rangle$ was estimated from $\langle\sigma_\theta\rangle = \Sigma\sigma_{\theta i}/N$, with $\sigma_{\theta\ i}$ as the uncertainty in *i*th polarization angle[12] and N as number of position angles.

The corrected value of dispersion in position angle σ_θ is found to be $\sim 15 \pm 2^\circ$ where uncertainty is measured as standard deviation in the distribution of measured uncertainties in the position angles. The turbulence in the DCF relation is measured by the dispersion in the line-of-sight velocity. Carney et al. (2016) has done a detailed investigation of kinematics in cloud condensations toward Taurus and Perseus star-forming regions using JCMT HARP observations of HCO^+ ($J = 4-3$) and $C^{18}O$ ($J = 3-2$) gas tracers. But the $C^{18}O$ ($J = 3-2$) line profiles are affected by the motions in the core envelope. Therefore we looked at the survey toward starless cores presented by Lee et al. (2001) using N_2H^+ (J = 1–0) lines. We have adopted the FWHM value of the N_2H^+ (J = 1–0) line ($\Delta v_{N_2H_+} = 0.37 \pm 0.02$ km s^{-1}) observed toward the L1521F core. This core was originally noticed as a dense condensation with a high central density of $\sim 10^6$ cm^{-3} (Onishi et al. 1999). Kirk et al. (2005) reported a volume density of L1521F core as 2×10^6 cm^{-3} with $\sim$50% uncertainty using JCMT/SCUBA mapping. We used the above values of standard deviation in polarization angles, dispersion in N_2H^+ (J = 1–0) line velocity and volume density in DCF relation and estimated the *B*-field strengths as $\sim 330 \pm 100$ μG in the core.

Plane-of-the-sky magnetic field strength estimation in the envelope of L1521F ($\sim$25 μG) by Soam et al. (2015) is found to be more than 10 times lower than the value we obtained at the core scale. This suggests a strengthening of *B*-fields in the subparsec scale from parsec scale. This may be caused by the dragging of field lines from the envelope to the core region. The line-of-sight *B*-field strength toward this core has been

[12] The uncertainty in the position angles is calculated by error propagation in the expression of polarization angle θ, which gives, $\sigma_\theta = 0.5 \times \sigma_P/P$ in radians, or $\sigma_\theta = 28.^\circ65 \times \sigma_P/P$ (see Serkowski 1974) in degrees.

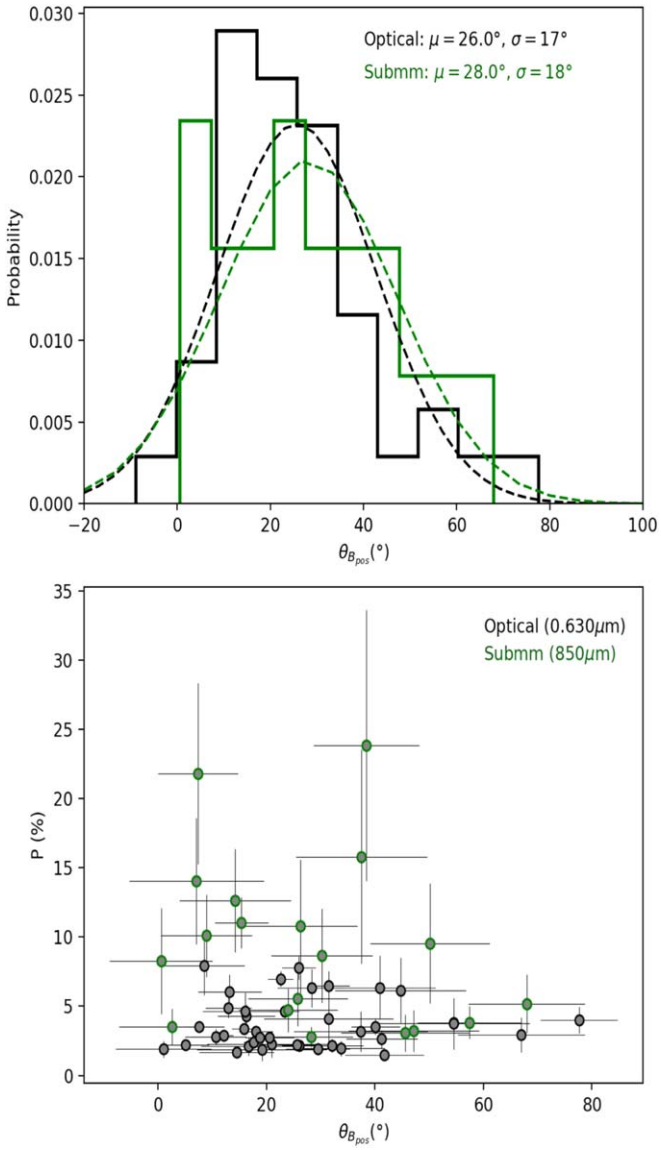

Figure 3. Upper panel: the Gaussian fitted histograms of plane-of-sky *B*-field position angles measured at optical (black) and submillimeter (green) wavelength toward L1521F. Lower panel: distribution of percentage of polarization with *B*-field position angles in the two samples.

found to be -1.4 ± 4.0 μG by Crutcher et al. (2010) using OH Zeeman observations from the Arecibo telescope. The plane-of-sky and line-of-sight magnetic field strengths suggest that the average *B*-field strength in the core is of the order of $\sim$330 μG.

3.4. Mass-to-flux Ratio

The mass-to-flux ratio estimation helps in testing the relative importance of gravity and magnetic fields in the molecular clouds. This parameter is represented by λ (Crutcher 2004). The core stability can be tested using the observed *B*-field strength and column density values. The H_2 column density of L1521F is found to be 1×10^{23} cm^{-2} by Kirk et al. (2005) from JCMT/SCUBA observations. We adopted this value of column density and the average magnetic field strength as $\sim$330 $\pm$ 100 μG in L1521F core. The value of λ is estimated

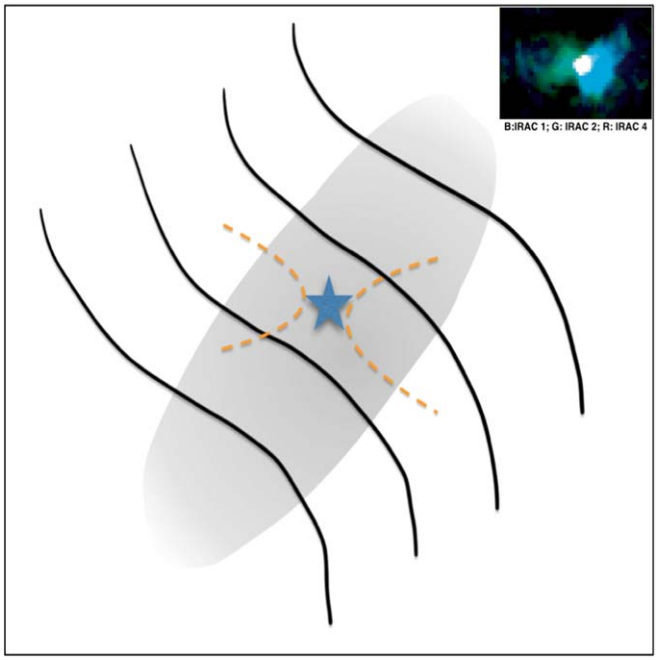

Figure 4. Cartoon showing the field lines, location of L1521F-IRS, and bipolar outflow cavities in L1521F. The inset in the upper right corner shows the *Spitzer* color-composite image obtained from Bourke et al. (2006).

using the relation given by Crutcher (2004)

$$\lambda = 7.6 \times 10^{-21} \frac{N(\mathrm{H_2})}{B_{\mathrm{pos}}}, \quad (2)$$

where $N(H_2)$ is the molecular hydrogen column density in cm^{-2} and B_{pos} is the plane-of-sky field strength in μG. For the considered values of B_{pos} and column density, we find $\lambda = 2.3 \pm 0.7$ where the error is included from the uncertainty in *B*-field strength measurement only. Since the plane-of-sky magnetic field is dominating toward L1521F, we are not applying any geometrical correction on the measured value of λ. This suggests that the core is super-critical, which is consistent with the asymmetric line profiles seen by Lee et al. (2001) predicting global infall motions in the core.

3.5. B-fields and Turbulence from Envelope to Core

A simple comparison of magnetic field strength and turbulence from parsec to subparsec scales can be done in L1521F using optical and submillimeter polarization results and line observations using CO ($J = 1$–0) in the diffuse envelope (Kim et al. 2019) and N_2H^+ ($J = 1$–0) in the dense core region (Lee et al. 2001). Since the plane-of-the-sky component of magnetic fields is much stronger than line-of-sight field strength, we assume the total field strength (B_{tot}) to be the same as the measured value of plane-of-the-sky *B*-field strength.

The total magnetic field energy (E_{mag}) can be calculated as

$$E_{\mathrm{mag}} = \frac{B_{\mathrm{tot}}^2 V}{2\mu_0}, \quad (3)$$

where V is the core volume ($=4/3 \times \pi r^3$) with r as the radius of core. μ_0 is the permeability of vacuum. We used the radius of the envelope as the extent to which optical polarization

Table 2
Values Calculated in L1521F Envelope and Core Regions

Region	B_{tot} (μG)	E_{mag} (J)	$E_{NT,\ kin}$ (J)
Envelope	25	1.3×10^{38}	1.9×10^{36}
Core	330	5.5×10^{35}	3.5×10^{34}

measurements are done. The core radius is estimated from the 850 μm continuum emission.

The nonthermal kinetic energy ($E_{NT,kin}$) of the envelope and core can be calculated as

$$E_{NT,kin} = \frac{3M\sigma_v^2}{2}, \quad (4)$$

where M is the mass of the core and σ_v is the average one-dimensional line-of-sight nonthermal velocity dispersion. We adopted the envelope mass from Kim et al. (2016), measured from available *Herschel*/SPIRE 250 or 500 μm fluxes. We estimated the core mass from observed 850 μm emission using the following relation (Hildebrand 1983)

$$M = \frac{S_\nu D d^2}{\kappa_\nu B_\nu(T)}, \quad (5)$$

where S_ν is the 850 μm flux density, D is the dust-to-gas mass ratio assumed as 0.01, d is the distance of the core (i.e., 140 pc), κ_ν is the dust opacity, which is adopted as 1.85 cm^2 g^{-1} from Ossenkopf & Henning (1994), and B_ν(T) is the Planck function. We assumed a core temperature of 9 K from the SCUBA observations of the L1521F at 850 μm (Kirk et al. 2005).

The values of B_{tot}, E_{mag}, and $E_{NT,kin}$ for L1521F envelope and core are given in Table 2. The magnetic energies in the envelope and core are 1–2 orders of magnitude higher than the nonthermal kinetic energies of these regions suggesting that magnetic fields are more important than turbulence and contributing more to the energy budget of L1521F.

3.6. Depolarization

We investigated the change in polarization fraction from diffuse to high-density regions on L1521F core as done in several other star-forming regions by previous studies (i.e., Matthews & Wilson 2000; Lai et al. 2001; Tang et al. 2013; Alves et al. 2014; Hull et al. 2017; Juvela et al. 2018; Koch et al. 2018). Top panel of Figure 5 shows the *B*-field geometry seen in L1521F core from POL-2 observations. The lengths of line segments are proportional to the polarization percentage. It can be noticed that the amount of polarization fraction decreases toward high-density brighter regions. The decrement can be quantified by comparing the length of line segments with scale bar. This phenomena is widely known as depolarization in molecular cloud cores. This variation of degree of polarization is further investigated in the lower panel of the figure which shows the variation of polarization fraction with intensity. This plot suggests that the core-scale fraction of polarization is decreasing with the intensity toward the higher density regions. We measured the power-law slope in the distribution using a least-squares fit, and found it to be $\alpha = -0.86$. The widely accepted possible reasons of lower observed polarization fraction in the cores include the changes

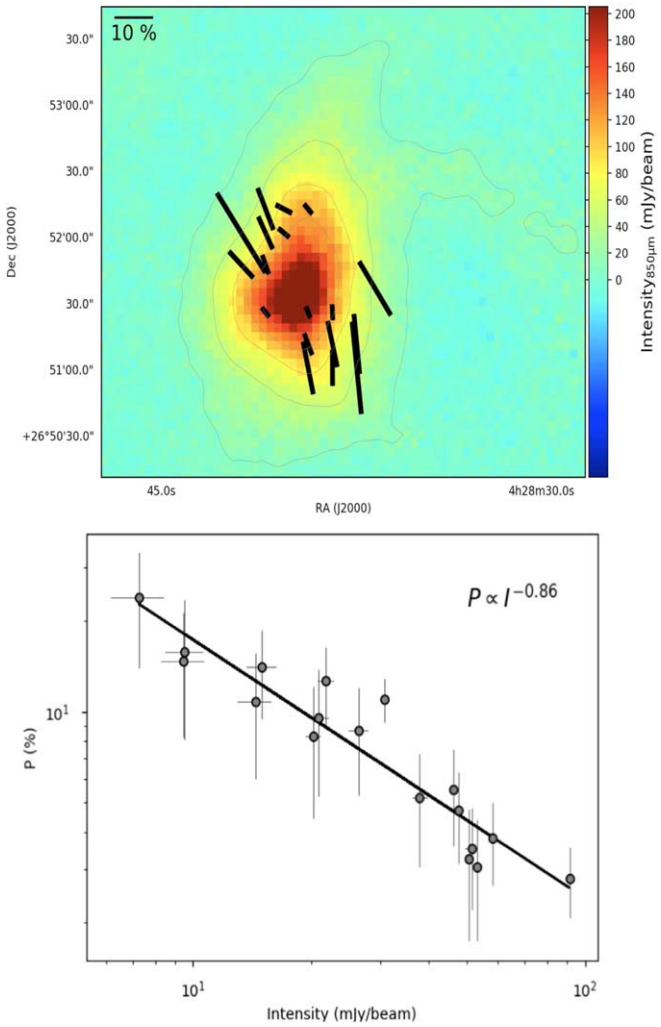

Figure 5. Upper panel: the *B*-field geometry observed from 850 μm POL-2 observations. The lengths of line segments are proportional to the polarization percentage. The scale for polarization fraction is also indicated. Lower panel: the variation of polarization fraction with the intensity in the L1521F core. The values and their uncertainties are taken from the POL-2 measurements with 12″ pixel size with a 3 × 3 binning.

in *B*-field orientation in the denser regions. These changes could also stem from the grain growth with a consequence of more spherical shapes thus not getting aligned with the *B*-fields. Other possible reasons of the change are suspected to be the magnetic reconnection (Lazarian & Vishniac 1999) and/or from weak radiative alignment torques (RATs; Lazarian & Hoang 2007) due to weak radiation field in dense regions. But the radiation from L1521F-IRS may compensate for the loss of interstellar radiation field and help in radiative alignment of the grains.

The power-law index in L1521F is found to be similar to the index $\alpha \sim -0.9$ in ρ Ophiuchus B (Soam et al. 2018) and more identical to $\alpha \sim -0.8$ in ρ Ophiuchus A (Kwon et al. 2018). A recent study by Seifried et al. (2018) explored the reasons of the observed depolarization in the center of molecular clouds using dust polarization maps of 3D magnetohydrodynamical (MHD) simulations. From the MHD modeling of their synthetic data, they found that dust grains remain aligned even at high densities ($>10^3$ cm^{-3}) and visual extinction of $A_V > 1$ mag. They suggest that depolarization is rather caused by

strong variations of the magnetic field direction along the line-of-sight due to turbulent motions.

Jones (1989) and Jones et al. (1992) assumed that magnetic field consists of a constant as well as a random component and modeled polarized radiation through an extended cloud. They found $\alpha = -0.5$ when random component dominates the magnetic field with expected polarization scales as the square root of number of turbulent cells. The values of slopes steeper than -0.5 leads to the prediction of more turbulent environment toward the central high-density regions of the cores. We tested this hypothesis on our results by checking the slope in the very center of the core. We considered the six data points with total intensities higher than 45 mJy beam^{-1} from the lower panel of Figure 5 for fitting power law. We obtained a slope of -0.47 in the central region which is much closer to the value found by Jones et al. (1992). The shallower nature of the P versus I distribution in central high-density region compared to the whole region suggests that the B-fields are stronger on the outer periphery and core is more turbulent toward the central high-density region causing scrambled B-fields and hence decrease in polarization due to beam averaging across lots of B-field orientations.

The turbulent nature of L1521F core is supported by several studies done to investigate the kinematics of this core using high-resolution ALMA observations (Tokuda et al. 2014, 2016, 2017, 2018). The mentioned studies found that L1521F is a site with high-dynamic gas interactions and a multiple star formation at a scale of ∼100 au. Tokuda et al. (2018) observed a ^{12}CO(J = 3–2) line in this core using ALMA at ∼20 au resolution and found complex warm filamentary/clumpy structures with the sizes from a few tens of astronomical units to ∼1000 au. These findings suggest that the plausible reason of depolarization seen toward L1521F may be the presence of enhanced turbulence in the central high-density region of the core.

3.7. Magnetic Fields in Other Cores with VeLLOs

The present study is the first subparsec scale observation of a nearby core with VeLLO using high-sensitivity POL-2 instrument as compared to the SCUPOL at JCMT. Prior to the investigation we presented in this work, there have been several attempts made for mapping B-fields in the low-mass star-forming cores. However, only one core with VeLLO namely IRAM 04191+1522 (hereafter IRAM04191) in Taurus has been observed with SCUPOL in a previous study by Matthews et al. (2009). We are considering this case with similar central source luminosity for the discussion in context with L1521F.

Soam et al. (2015) have mapped the B-fields in the envelopes of five cores with VeLLOs using optical polarization measurements. Polarization measurements toward IRAM04191 have been done in optical (Soam et al. 2015) and 850 μm (Matthews et al. 2009) wavelengths. The mean values of the polarization fraction and the magnetic field orientation with corresponding standard deviations in IRAM04191 are found to be $13 \pm 7\%$ and $32^\circ \pm 36^\circ$ using SCUPOL. It can be noticed from Soam et al. (2015) and this work, that B-field line changes their direction by almost 90° in IRAM04191 whereas they are slightly bent in L1521F. This can be attributed to the different environments and kinematics of the two cores.

A highly collimated CO bipolar outflow was found to be associated with VeLLO embedded in IRAM04191 (André et al. 1999). From the CO map of the region presented by Belloche et al. (2002), the outflow direction is found to be 28° in the plane of the sky from north toward east. The inner B-fields mapped with SCUPOL observations are found to be almost aligned with the outflows in IRAM04191. However, the outflows and core magnetic fields in L1521F are found to be misaligned with an offset of ∼48°.

The VeLLOs are supposed to preserve their inherent B-fields in the parent cores as they are sources at the lowest end of the mass spectrum and the force from their associated bipolar outflows is found to be much smaller compared to other class 0 sources (Kim et al. 2019). This investigation can be done by plotting the variation of offsets between B-field orientation and outflow directions in these sources. Soam et al. (2017) has studied the detailed distribution of offsets between B-fields (inferred from optical polarization) and outflows with their corresponding outflow force values in several VeLLOs (shown in their Figure 10). The outflows are found to be misaligned (∼48°) in L1521F but aligned (∼4°) in IRAM04191. We need to increase the sample of such studies to arrive at any statistically significant conclusion of relation between outflow directions and magnetic field orientations.

4. Summary

1. We present results from the first sub-parsec-scale continuum polarization observation of L1521F, a core with an embedded VeLLO, now identified as a proto-brown dwarf candidate. The B-fields are found to be very well connected to the large-scale field structures seen in *Planck* dust polarization and optical polarization measurements suggesting the core embedded in the strong magnetic field region. The pronounced large-scale field lines seem to be running in the northeast and southwest direction.
2. The 850 μm continuum map interestingly shows two diffused elongated structures coming out of the main L1521F core.
3. The inner B-fields mapped with SCUPOL observations are found to be almost aligned with the outflows in IRAM04191. However, the outflows and core magnetic fields in L1521F are found to be misaligned with an offset of ∼48°.
4. The B-field strength in the L1521F core is estimated to be $\sim 330 \pm 100$ μG, which is more than 10 times larger than the value estimated in the envelope. The core is found to be super-critical with a λ value of 2.3 ± 0.7.
5. The magnetic energies in the envelope and core are 1–2 orders of magnitude higher than the nonthermal kinetic energies of these regions making magnetic fields contribute more to the energy budget of L1521F.
6. The fraction of polarization as a function of total intensity is found to be decreasing in the denser region, suggesting depolarization in the core with a power-law slope of $\alpha = -0.86$.

The authors thank the referee for constructive comments and suggestions that helped to improve the content of the manuscript. A.S. and B-G.A. are supported by NSF Grant-1715876. A.S. carried out this work in part at the Korea Astronomy & Space Science Institute (KASI) with support from the KASI postdoctoral fellowship. T.L. is supported by KASI and EACOA fellowships. M.J. acknowledges the support of Academy of Finland grant 1285769. C.W.L. is supported by the Basic Science Research Program through the National Research Foundation of Korea (NRF) funded by the Ministry of Education, Science and

Technology (NRF-2019R1A2C1010851). W.K. was supported by Basic Science Research Program through the National Research Foundation of Korea (NRF-2016R1C1B2013642). A.S. thanks P. Bhardwaj and Simon Coudé for the discussion during the analysis work. JCMT is operated by the East Asian Observatory on behalf of the National Astronomical Observatory of Japan; Academia Sinica Institute of Astronomy and Astrophysics; the Korea Astronomy and Space Science Institute; the Operation, Maintenance and Upgrading Fund for Astronomical Telescopes and Facility Instruments, budgeted from the Ministry of Finance of China and administrated by the Chinese Academy of Sciences and, the National Key R&D Program of China (No. 2017YFA0402700).

Facility: James Clerk Maxwell telescope (JCMT).

Softwares: Starlink (Currie et al. 2014), Astropy (Astropy Collaboration et al. 2013).

ORCID iDs

Archana Soam https://orcid.org/0000-0002-6386-2906
Chang Won Lee https://orcid.org/0000-0002-3179-6334
B-G Andersson https://orcid.org/0000-0001-6717-0686
Mika Juvela https://orcid.org/0000-0002-5809-4834
Tie Liu https://orcid.org/0000-0002-5286-2564
Gwanjeong Kim https://orcid.org/0000-0003-2011-8172
Ramprasad Rao https://orcid.org/0000-0002-1407-7944
Eun Jung Chung https://orcid.org/0000-0003-0014-1527
Woojin Kwon https://orcid.org/0000-0003-4022-4132

References

Allen, A., Li, Z.-Y., & Shu, F. H. 2003, ApJ, 599, 363
Alves, F. O., Frau, P., Girart, J. M., et al. 2014, A&A, 569, L1
André, P., Motte, F., & Bacmann, A. 1999, ApJL, 513, L57
Astropy Collaboration, Robitaille, T. P., Tollerud, E. J., et al. 2013, A&A, 558, A33
Beichman, C. A., Myers, P. C., Emerson, J. P., et al. 1986, ApJ, 307, 337
Belloche, A., André, P., Despois, D., & Blinder, S. 2002, A&A, 393, 927
Benson, P. J., & Myers, P. C. 1989, ApJS, 71, 89
Bourke, T. L., Myers, P. C., Evans, N. J., II, et al. 2006, ApJL, 649, L37
Carney, M. T., Yıldız, U. A., Mottram, J. C., et al. 2016, A&A, 586, A44
Chandrasekhar, S., & Fermi, E. 1953, ApJ, 118, 113
Chapin, E. L., Berry, D. S., Gibb, A. G., et al. 2013, MNRAS, 430, 2545
Codella, C., Welser, R., Henkel, C., Benson, P. J., & Myers, P. C. 1997, A&A, 324, 203
Crutcher, R. M. 2004, Ap&SS, 292, 225
Crutcher, R. M., Nutter, D. J., Ward-Thompson, D., & Kirk, J. M. 2004, ApJ, 600, 279
Crutcher, R. M., Troland, T. H., Goodman, A. A., et al. 1993, ApJ, 407, 175
Crutcher, R. M., Wandelt, B., Heiles, C., Falgarone, E., & Troland, T. H. 2010, ApJ, 725, 466
Currie, M. J., Berry, D. S., Jenness, T., et al. 2014, in ASP Conf. Ser. 485, Astronomical Data Analysis Software and Systems XXIII, ed. N. Manset & P. Forshay (San Francisco, CA: ASP), 391
Davis, L. 1951, PhRv, 81, 890
Dobashi, K., Uehara, H., Kandori, R., et al. 2005, PASJ, 57, S1
Franco, G. A. P., Alves, F. O., & Girart, J. M. 2010, ApJ, 723, 146
Friberg, P., Bastien, P., Berry, D., et al. 2016, Proc. SPIE, 9914, 991403
Goodman, A. A. 1996, in ASP Conf. Ser. 97, Polarimetry of the Interstellar Medium, ed. W. G. Roberge & D. C. B. Whittet (San Francisco, CA: ASP), 325
Goodman, A. A., Jones, T. J., Lada, E. A., & Myers, P. C. 1995, ApJ, 448, 748
Heiles, C. 2000, AJ, 119, 923
Hildebrand, R. H. 1983, QJRAS, 24, 267
Hoang, T., & Lazarian, A. 2008, MNRAS, 388, 117
Holland, W. S., Bintley, D., Chapin, E. L., et al. 2013, MNRAS, 430, 2513
Hull, C. L. H., Girart, J. M., Tychoniec, Ł., et al. 2017, ApJ, 847, 92
Jenness, T., Chapin, E. L., Berry, D. S., et al. 2013, SMURF: SubMillimeter User Reduction Facility, Astrophysics Source Code Library, ascl:1310.007
Jones, T. J. 1989, ApJ, 346, 728
Jones, T. J., Klebe, D., & Dickey, J. M. 1992, ApJ, 389, 602
Juvela, M., Guillet, V., Liu, T., et al. 2018, A&A, 620, A26
Kauffmann, J., Bertoldi, F., Bourke, T. L., Evans, N. J., II, & Lee, C. W. 2008, A&A, 487, 993
Kim, G., Lee, C. W., Maheswar, G., et al. 2019, ApJS, 240, 18
Kim, M.-R., Lee, C. W., Dunham, M. M., et al. 2016, ApJS, 225, 26
Kirk, J. M., Ward-Thompson, D., & André, P. 2005, MNRAS, 360, 1506
Kirk, J. M., Ward-Thompson, D., & André, P. 2007, MNRAS, 375, 843
Koch, P. M., Tang, Y.-W., Ho, P. T. P., et al. 2018, ApJ, 855, 39
Krumholz, M. R., McKee, C. F., & Klein, R. I. 2005, Natur, 438, 332
Kwon, J., Doi, Y., Tamura, M., et al. 2018, ApJ, 859, 4
Lai, S.-P., Crutcher, R. M., Girart, J. M., & Rao, R. 2001, ApJ, 561, 864
Lazarian, A., & Hoang, T. 2007, MNRAS, 378, 910
Lazarian, A., & Vishniac, E. T. 1999, ApJ, 517, 700
Lee, C. W., Kim, M.-R., Kim, G., et al. 2013, ApJ, 777, 50
Lee, C. W., Myers, P. C., & Tafalla, M. 1999, ApJ, 526, 788
Lee, C. W., Myers, P. C., & Tafalla, M. 2001, ApJS, 136, 703
Liu, T., Zhang, Q., Kim, K.-T., et al. 2016, ApJS, 222, 7
Loinard, L., Mioduszewski, A. J., Rodríguez, L. F., et al. 2005, ApJL, 619, L179
Mairs, S., Johnstone, D., Kirk, H., et al. 2015, MNRAS, 454, 2557
Matthews, B. C., McPhee, C. A., Fissel, L. M., & Curran, R. L. 2009, ApJS, 182, 143
Matthews, B. C., & Wilson, C. D. 2000, ApJ, 531, 868
McKee, C. F., Zweibel, E. G., Goodman, A. A., & Heiles, C. 1993, in Protostars and Planets III, ed. E. H. Levy & J. I. Lunine (Tucson, AZ: Univ. Arizona Press), 327
Mouschovias, T. C., & Ciolek, G. E. 1999, in NATO ASIC Proc. 540: The Origin of Stars and Planetary Systems, ed. C. J. Lada & N. D. Kylafis (Dordrecht: Kluwer), 305
Onishi, T., Mizuno, A., & Fukui, Y. 1999, PASJ, 51, 257
Ossenkopf, V., & Henning, T. 1994, A&A, 291, 943
Ostriker, E. C., Stone, J. M., & Gammie, C. F. 2001, ApJ, 546, 980
Pineda, J. E., Arce, H. G., Schnee, S., et al. 2011, ApJ, 743, 201
Planck Collaboration, Adam, R., Ade, P. A. R., et al. 2016, A&A, 594, A1
Seifried, D., Walch, S., Haid, S., Girichidis, P., & Naab, T. 2018, ApJ, 855, 81
Serkowski, K. 1974, in Astrophysics. Part A: Optical and infrared, ed. N. P. Carleton (New York: Academic Press), 361
Shimajiri, Y., André, P., Palmeirim, P., et al. 2019, A&A, 623, A16
Shu, F. H., Adams, F. C., & Lizano, S. 1987a, ARA&A, 25, 23
Shu, F. H., Lizano, S., & Adams, F. C. 1987b, in IAU Symp. 115, Star-forming Regions, ed. M. Peimbert & J. Jugaku (Dordrecht: Reidel), 417
Soam, A., Lee, C. W., Maheswar, G., et al. 2017, MNRAS, 464, 2403
Soam, A., Maheswar, G., Lee, C. W., et al. 2015, A&A, 573, A34
Soam, A., Pattle, K., Ward-Thompson, D., et al. 2018, ApJ, 861, 65
Takahashi, S., Ohashi, N., & Bourke, T. L. 2013, ApJ, 774, 20
Tan, J. C., Krumholz, M. R., & McKee, C. F. 2006, ApJL, 641, L121
Tang, Y.-W., Ho, P. T. P., Koch, P. M., Guilloteau, S., & Dutrey, A. 2013, ApJ, 763, 135
Terebey, S., Van Buren, D., Brundage, M., & Hancock, T. 2006, ApJ, 637, 811
Tokuda, K., Onishi, T., Matsumoto, T., et al. 2016, ApJ, 826, 26
Tokuda, K., Onishi, T., Saigo, K., et al. 2014, ApJL, 789, L4
Tokuda, K., Onishi, T., Saigo, K., et al. 2017, ApJ, 849, 101
Tokuda, K., Onishi, T., Saigo, K., et al. 2018, ApJ, 862, 8
Torres, R. M., Loinard, L., Mioduszewski, A. J., & Rodríguez, L. F. 2007, ApJ, 671, 1813
Ward-Thompson, D., Sen, A. K., Kirk, J. M., & Nutter, D. 2009, MNRAS, 398, 394
Wu, Y., Wei, Y., Zhao, M., et al. 2004, A&A, 426, 503